




# Low-temperature diffusion in thin-film Pt-(Au)-Co heterostructures: a structural and magnetic characterization

Roman Pedan<sup>1</sup>, Pavlo Makushko<sup>2</sup>, Yurii Yavorskyi<sup>1</sup>,  
Oleksandr Dubikovskiy<sup>1,3</sup>, Andrii Bodnaruk<sup>1,4</sup>, Andrii Burmak<sup>1</sup>,  
Vladimir Golub<sup>5</sup>, Svitlana Voloshko<sup>1</sup>, René Hübner<sup>2</sup> ,  
Denys Makarov<sup>2,\*</sup>  and Igor Vladymyrskyi<sup>1,\*</sup> 

<sup>1</sup> National Technical University of Ukraine ‘Igor Sikorsky Kyiv Polytechnic Institute’, Prospect Beresteyskyi 37, Kyiv 03056, Ukraine

<sup>2</sup> Helmholtz-Zentrum Dresden-Rossendorf e.V., Institute of Ion Beam Physics and Materials Research, D-01328 Dresden, Germany

<sup>3</sup> V. Lashkaryov Institute of Semiconductor Physics, National Academy of Sciences of Ukraine, Prospect Nauky 41, Kyiv 03680, Ukraine

<sup>4</sup> Institute of Physics, National Academy of Sciences of Ukraine, Prospect Nauky 46, Kyiv 03028, Ukraine

<sup>5</sup> Institute of Magnetism, National Academy of Sciences of Ukraine and Ministry of Education and Science of Ukraine, 36-B Vernadsky Blvd., Kyiv 03142, Ukraine

E-mail: [d.makarov@hzdr.de](mailto:d.makarov@hzdr.de) and [vladymyrskyi@kpm.kpi.ua](mailto:vladymyrskyi@kpm.kpi.ua)

Received 4 October 2023, revised 11 January 2024

Accepted for publication 24 January 2024

Published 21 February 2024



CrossMark

## Abstract

Formation of functional thin films for nanoelectronics and magnetic data storage via thermally induced diffusion-driven structural phase transformations in multilayer stacks is a promising technology-relevant approach. Ferromagnetic thin films based on Co Pt alloys are considered as a material science platform for the development of various applications such as spin valves, spin orbit torque devices, and high-density data storage media. Here, we study diffusion processes in Pt–Co-based stacks with the focus on the effect of layers inversion (Pt/Co/substrate versus Co/Pt/substrate) and insertion of an intermediate Au layer on the structural transitions and magnetic properties. We demonstrate that the layer stacking has a pronounced effect on the diffusion rate at temperatures, where the diffusion is dominated by grain boundaries. We quantify effective diffusion coefficients, which characterize the diffusion rate of Co and Pt through the interface and grain boundaries, providing the possibility to control the homogenization rate of the Pt–Co-based heterostructures. The obtained values are in the range of  $10^{-16}$ – $10^{-13}$   $\text{cm}^2 \text{s}^{-1}$  for temperatures of 150 °C–350 °C. Heat treatment of the thin-film samples results in the coercivity enhancement, which is attributed to short-range chemical ordering effects. We show that introducing an additional Au intermediate layer leads to an increase of the coercive field of the annealed samples due to a modification of exchange coupling between the magnetic grains at the grain boundaries.

Supplementary material for this article is available [online](#)

\* Authors to whom any correspondence should be addressed.



Original content from this work may be used under the terms of the [Creative Commons Attribution 4.0 licence](#). Any further distribution of this work must maintain attribution to the author(s) and the title of the work, journal citation and DOI.

Keywords: Co–Pt alloy, grain boundary diffusion, magnetic thin films, short-range chemical order, diffusion coefficient

## 1. Introduction

Magnetic thin films play a decisive role in magnetic data storage and numerous sensor applications. For instance, ferromagnetic chemically ordered  $L1_0$ -CoPt thin films are promising candidate materials for magnetic tunnel junctions [1, 2], high-density hard disk drives [3], nanoscaled permanent magnets [4], and exchange-coupled composites [5, 6]. In particular, recent studies of CoPt alloys are devoted to their application as spin valves and transistors [7–10], spin orbit torque devices [11], investigation of magneto-plasmonic phenomena [12, 13], and skyrmions formation [14]. In addition to chemically ordered CoPt alloys, their chemically disordered counterparts (i.e. A1-CoPt) reveal current-induced magnetization switching in a perpendicularly magnetized single layer [15]. These experimental advances motivate active theoretical research on CoPt alloys confirming that the magnetocrystalline anisotropy energy of this alloy could be controlled by tetragonal distortion of the lattice [16].

Typically, CoPt-based ferromagnetic nanomaterials are prepared by deposition of the CoPt alloy followed by an annealing process [17–21] or via thin-film growth on heated substrates [22]. To control the crystal orientations and achieve perpendicular magnetic anisotropy, single-crystal substrates, e.g.  $\text{Al}_2\text{O}_3(0001)$  [23],  $\text{SrTiO}_3(001)$  [24], and  $\text{MgO}(001)$  [25, 26], are typically used for the growth of CoPt films. A possibility to form  $L1_0$ -CoPt thin films using cost-efficient  $\text{SiO}_2/\text{Si}(001)$  substrates is also explored [27, 28]. It is important to note that the fabrication temperatures needed for these approaches are relatively high ( $\sim 700^\circ\text{C}$ – $800^\circ\text{C}$ ) and governed by bulk diffusion processes.

The formation of functional thin films by thermally induced diffusion processes in layered stacks obtained by consequential deposition of separate layers is an alternative fabrication route. This approach offers an appealing benefit that the structural phase transitions and related phase formation in the stack are achieved at relatively low temperatures, providing conditions for diffusion development primarily by the grain boundary mechanism [29]. In this case, intermetallic compounds are formed via solid-state reactions driven by grain boundary diffusion: boundaries saturated by the diffusant could move in the direction perpendicular to their initial plane leaving behind an area of the formed phase [30].

Various intermetallic phases were successfully realized via diffusion activation in layered systems. For instance, diffusion-controlled phase formation was investigated for Ni–Al [31, 32], Ti–Zn [33], and Al–Ti [34]. This approach is explored for magnetic thin films as well. In particular, FePt homogeneous thin films were prepared as a result of low-temperature annealing of Pt/Fe bilayers, activating mass transfer via grain boundaries [30]. Moreover, layer stack inversion as well as introducing additional layers could lead to the enhancement of the diffusion rate due to additional stresses at the interfaces [35].

Recent studies showed that CoPt thin films can be formed via thermally induced structural phase transitions in Co/Pt-based layered stacks. Toyama *et al* reported the formation of the  $L1_0$  CoPt phase with a coercivity of 2.1 kOe by rapid thermal annealing at  $900^\circ\text{C}$  for 30 s of Co(4.8 nm)/Pt(6.6 nm) bilayers [36]. Furthermore,  $L1_0$ -CoPt ordered thin films with a coercivity of 13kOe were obtained by annealing  $[\text{Co}/\text{Pt}]_{4x}$  multilayers in  $\text{Ar}+\text{H}_2$  forming gas at  $700^\circ\text{C}$ – $900^\circ\text{C}$  for 10–90 min [37]. We reported the realization of homogeneous CoPt alloy thin films via annealing of Pt/Co stacks at temperatures below  $500^\circ\text{C}$  resulting in the formation of a disordered A1-CoPt phase [38], where the hard-magnetic properties of the A1-CoPt thin films were linked to a short-range chemical ordering effect.

The development of reliable protocols of thin-films formation driven by diffusion-controlled structural phase transitions in layered stacks requires the determination of the diffusion parameters. This is an important task of fundamental material science aimed to control homogenization processes and ordering rates upon the formation of functional materials. However, for nanoscale films, there are numerous issues with the estimation of the diffusion parameters. This is caused by different diffusion mechanisms (e.g. surface, triple junctions, grain boundaries, bulk) which can contribute simultaneously to the mass transfer, the presence of moving grain boundaries, diffusant accumulation at the free surface, near substrate region and other interfaces to name just a few [29, 39–41]. So far, there have been no reports on the estimation of diffusion parameters in Co/Pt-based thin-film stacks, which motivates quantitative characterization of diffusion and diffusion-controlled phase formation in these functional materials.

Here, we report the effect of layer stacking (Pt/Co/substrate versus Co/Pt/substrate) and introducing an additional Au layer on the diffusion development and phase transitions in the Pt/Co-based films prepared on  $\text{SiO}_2/\text{Si}(001)$  substrates and subjected to annealing in vacuum. We quantify the interface, grain boundary, and effective diffusion parameters. This estimation allows us predicting the rate of low-temperature chemical composition homogenization of the Pt/Co-based heterostructures. It was found that inversion of the layer stack (Pt/Co versus Co/Pt) has significant effect on the diffusion homogenization rate at annealing up to some critical temperature, which is attributed to the modification of the dominating diffusion mechanism (from grain boundary to bulk) and the development of mechanical stresses. Magnetic properties of the studied samples are reported as well.

## 2. Experimental procedure

Magnetron sputtering was used to deposit 4 families of layer stacks including Co(10 nm)/Pt(10 nm)/substrate, Pt(10 nm)/Co(10 nm)/substrate, Co(10 nm)/Au(2 nm)/Pt(10 nm)/substrate, and Pt(10 nm)/Au(2 nm)/Co(10 nm)/substrate. The

thickness of the individual layers is refined by cross-sectional transmission electron microscopy (TEM) imaging. The calculated average composition after complete homogenization of the bi-layered (Co/Pt/substrate and Pt/Co/substrate) stack with investigated layers thickness is  $\text{Co}_{0.58}\text{Pt}_{0.42}$ . The deposition process was performed at room temperature onto thermally oxidized  $\text{SiO}_2/\text{Si}(001)$  substrates (base pressure:  $5 \times 10^{-8}$  mbar; sputter Ar pressure:  $8 \times 10^{-4}$  mbar; deposition rate:  $2 \text{ \AA s}^{-1}$  for Co,  $1.5 \text{ \AA s}^{-1}$  for Pt,  $4 \text{ \AA s}^{-1}$  for Au). Co and Au are DC-sputtered; Pt is RF-sputtered. The as-deposited stacks were annealed in vacuum of  $10^{-6}$  mbar in the temperature range  $150 \text{ }^\circ\text{C}$ – $550 \text{ }^\circ\text{C}$  with a constant annealing duration of 30 min. Annealing at various temperatures with constant duration enables the estimation of the diffusion parameters for different diffusion mechanisms. The highest annealing temperature assures homogenization of the chemical composition through the whole stack [38]. The phase composition of the as-deposited and annealed stacks was analyzed by x-ray diffraction (XRD) in  $\theta$ – $2\theta$  geometry using a Rigaku Ultima IV diffractometer with  $\text{CuK}\alpha$  radiation source. Diffraction peaks were fitted by PseudoVoigt functions allowing to extract their center of gravity positions and calculate the lattice parameters of the formed phases. Bright-field (BF), annular dark-field (ADF), and high-angle annular dark-field (HAADF) scanning transmission electron microscopy (STEM) imaging as well as spectrum imaging analysis based on energy-dispersive x-ray spectroscopy (EDXS) were done with a Talos F200X microscope operated at an accelerating voltage of 200 keV and equipped with a Super-X EDXS detector system (FEI). Secondary ion mass spectrometry (SIMS) analysis was used to perform chemical depth profiling of the stacks. For these measurements, an Ion Tof IV device with a primary beam of negative  $\text{Cs}^-$  (2 keV) ions was employed. The interface (by Hall–Morabito method), grain boundary (by Fisher–Whipple approach), and effective diffusion coefficients were estimated based on the measured SIMS chemical depth profiles. Magnetic characterization of the samples was performed at room temperature by vibrating sample magnetometry (VSM) and ferromagnetic resonance measurements using a Bruker ELEXYS-E500 X-band (9.86 GHz) spectrometer.

### 3. Results and discussion

#### 3.1. Structural characterization

Figure 1 shows the XRD patterns of the investigated stacks in the as-deposited state and after annealing in the temperature range of  $350 \text{ }^\circ\text{C}$ – $550 \text{ }^\circ\text{C}$  for 30 min. The diffractogram of each as-deposited stack reveals the presence of a peak at about  $39.8^\circ$  corresponding to the set of Pt {111} lattice planes. The width of the Pt 111 peak depends on the stacking. Estimation of the Pt grain size in the as-deposited samples based on the Scherrer equation shows that the Pt grains are larger in case of the stacks with Co top layer ( $11.8 \pm 0.7$  nm for both Co/Pt/substrate and Co/Au/Pt/substrate stacks)

compared to stacks with Co bottom layer ( $9.9 \pm 0.7$  nm for Pt/Co/substrate and  $10.6 \pm 0.7$  nm for Pt/Au/Co/substrate). The error bars of the crystallite size estimation are provided based on the calculated instrumental broadening of the diffraction peaks. Moreover, the diffraction patterns of the as-deposited Co/Pt/substrate (figure 1(a)) and Co/Au/Pt/substrate (figure 1(c)) stacks, where Co is the top layer, reveal a weak diffraction peak at  $2\theta \approx 44.5^\circ$ , which is attributed to the hcp Co (002) plane. The angular position of the peak agrees well with hcp Co according to the PDF4+ database, which is in line with the literature data on Co thin films grown at low temperatures. The weak intensity of the Co peak for the XRD patterns of the stacks with Co top layer and its complete absence in case of the Pt/Co/substrate and Pt/Au/Co/substrate stacks (figures 1(b), (d)) could be attributed to a small size of Co grains in the corresponding layers, which is at the limit of the sensitivity of the XRD device. In addition, the diffraction patterns of the as-deposited Co/Au/Pt/substrate and Pt/Au/Co/substrate samples with intermediate Au layer (figures 1(c), (d)) are characterized by the appearance of a weak Au 111 diffraction peak at  $2\theta \approx 38.5^\circ$ . The presence of diffraction peaks from the pure metals in the XRD patterns of all as-deposited layer stacks confirms their crystalline state after magnetron sputtering.

Heat treatment of the samples at temperatures below  $350 \text{ }^\circ\text{C}$  does not lead to noticeable modifications of the XRD patterns (supplementary information, figure S1). Annealing at  $350 \text{ }^\circ\text{C}$  results in a decrease of the intensity of the Pt 111 peak accompanied by its broadening for each sample. We associate the appearance of the peak broadening (shoulder) with the onset of diffusion processes and the formation of a disordered A1-CoPt phase (the lattice parameter of A1-CoPt phase is close to the one of Pt). With an increase of the amount of the formed A1-CoPt phase, the peak shifts towards higher angles. Moreover, the diffraction pattern of the Pt/Au/Co/substrate sample after annealing at  $350 \text{ }^\circ\text{C}$  reveals an enhancement of the Au 111 peak intensity. An increase of the annealing temperature to  $450 \text{ }^\circ\text{C}$  leads to drastic structure modifications of each sample: a further decrease of the Pt 111 peak intensity is observed as well as a new peak appears at  $2\theta \approx 42^\circ$ , indicating the formation of the disordered A1-CoPt phase. Also, the increase of the Au 111 peak intensity is observed in the XRD patterns of the stacks containing an additional Au layer, which could be related to the diffusion of Au towards the free surface with the formation of surface segregation regions. After heat treatment at  $350 \text{ }^\circ\text{C}$  and  $450 \text{ }^\circ\text{C}$ , the Pt 111 and A1-CoPt 111 peak superimpose, as confirmed by the refinement analysis using PseudoVoigt functions (figure 2). An increase in the annealing temperature to  $550 \text{ }^\circ\text{C}$  is accompanied by further enhancement of the A1-CoPt 111 and Au 111 peak intensities indicating further development of the A1-CoPt phase and Au regions at the free surface, interface with the substrate, and grain boundaries. Moreover, after annealing at  $550 \text{ }^\circ\text{C}$ , the A1-CoPt 200 peak is additionally observed. The intensity of the Pt 111 peak becomes almost equal to the background, suggesting the absence of pure Pt in these annealed stacks. Based on the XRD data, we calculated the crystal structure parameters of the formed phases (table 1).

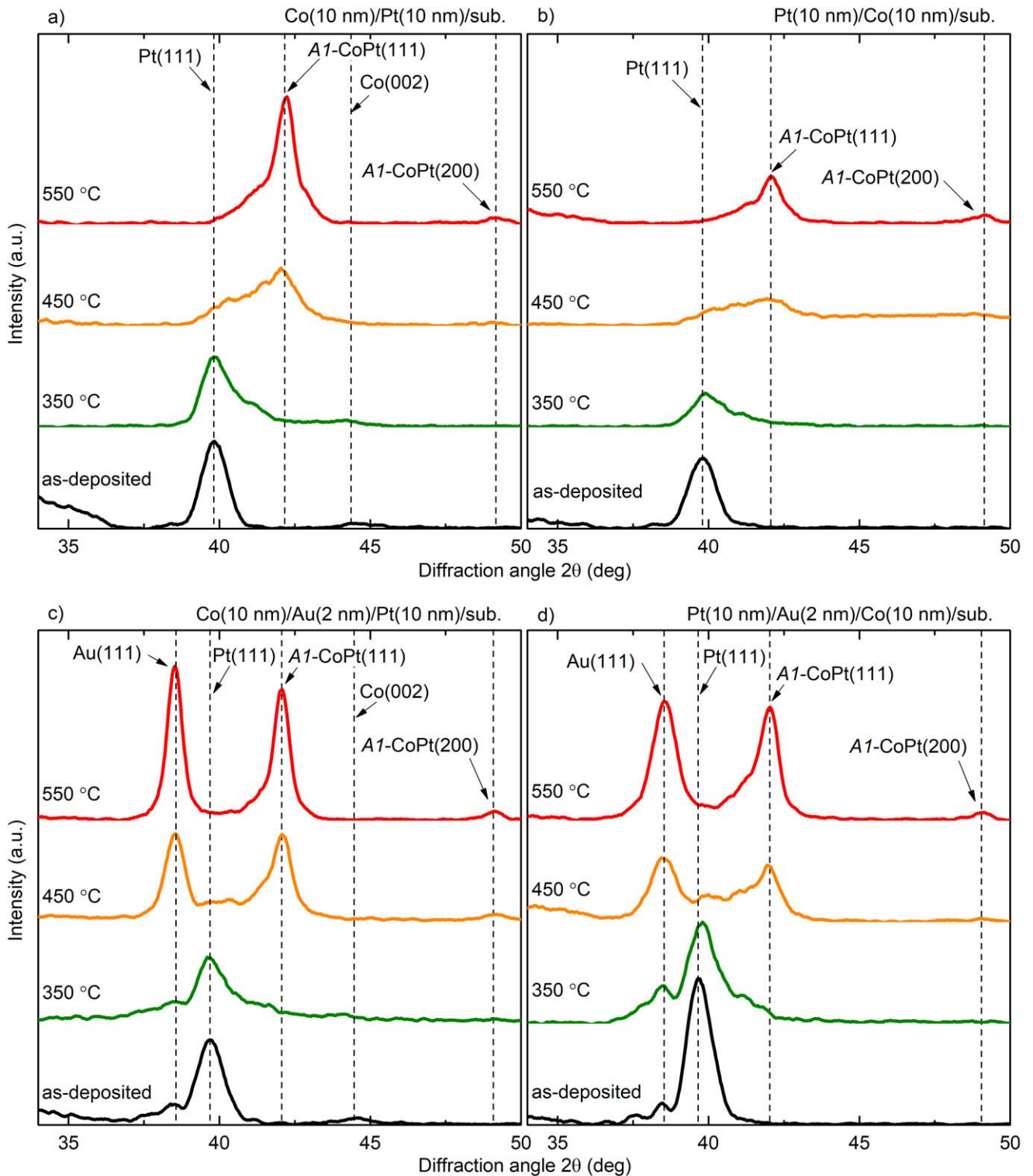


**Figure 1.** XRD patterns of the Co(10 nm)/Pt(10 nm)/substrate (a), Pt(10 nm)/Co(10 nm)/substrate (b), Co(10 nm)/Au(2 nm)/Pt(10 nm)/substrate (c), and Pt(10 nm)/Au(2 nm)/Co(10 nm)/substrate (d) stacks in the as-deposited state and after annealing in the temperature range 350 °C–550 °C for 30 min. ‘sub’ stands for the SiO<sub>2</sub>/Si substrate.

Figure 3 compares representative cross-sectional BF-STEM images and the corresponding EDXS-based element distribution maps of the as-deposited samples. The images confirm the layer setup and reveal a distinct separation

between the Co, Au, and Pt layers. It should be noted that the images of the Co/Pt/substrate and Co/Au/Pt/substrate stacks do not show the actual thickness of the Co layer but include a 2–3 nm thick Co oxide on top. Since the element

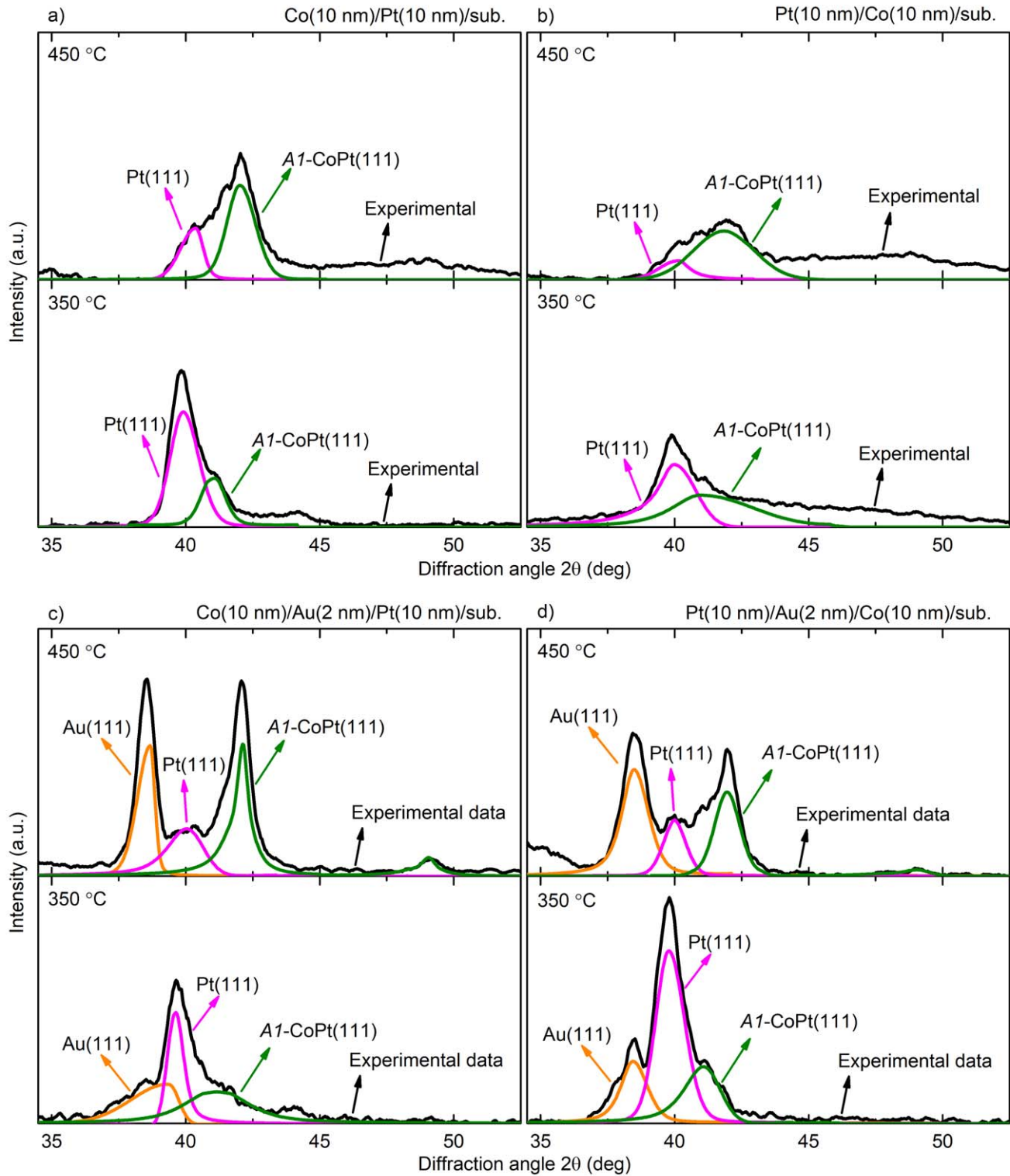


**Figure 2.** XRD patterns of the Co(10 nm)/Pt(10 nm)/substrate (a), Pt(10 nm)/Co(10 nm)/substrate (b), Co(10 nm)/Au(2 nm)/Pt(10 nm)/substrate (c), and Pt(10 nm)/Au(2 nm)/Co(10 nm)/substrate (d) stacks after annealing to 350 °C and 450 °C for 30 min with deconvolution of the peaks. 'sub' stands for the SiO<sub>2</sub>/Si substrate.

distribution maps in figure 3 were obtained at positions with larger TEM lamella thickness to get reasonable EDXS signals, the interface roughness between the single layers appears slightly broadened.

Figure 4 shows SIMS chemical depth profiles of the as-deposited samples and after annealing at 350 °C and 550 °C (SIMS profiles of the stacks treated at the other temperatures are given in the supplementary information, figures S3–S6).

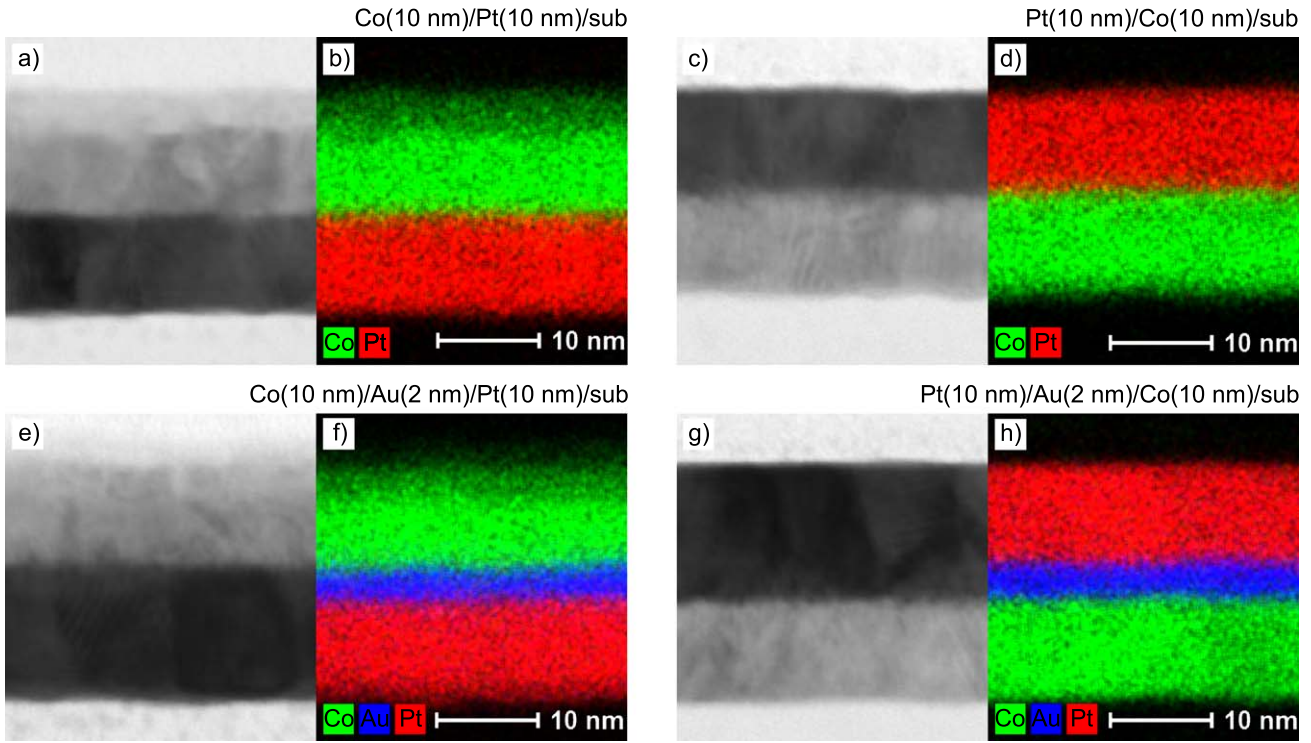


**Figure 3.** Cross-sectional BF-STEM images and corresponding EDXS-based element distribution maps of the as-deposited (a), (b) Co(10 nm)/Pt(10 nm)/substrate, (c), (d) Pt(10 nm)/Co(10 nm)/substrate, (e), (f) Co(10 nm)/Au(2 nm)/Pt(10 nm)/substrate, and (g), (h) Pt(10 nm)/Au(2 nm)/Co(10 nm)/substrate stacks.

**Table 1.** Lattice parameters of Co, Pt, Au, and Al-CoPt phases of the as-deposited samples and after annealing at various temperatures.

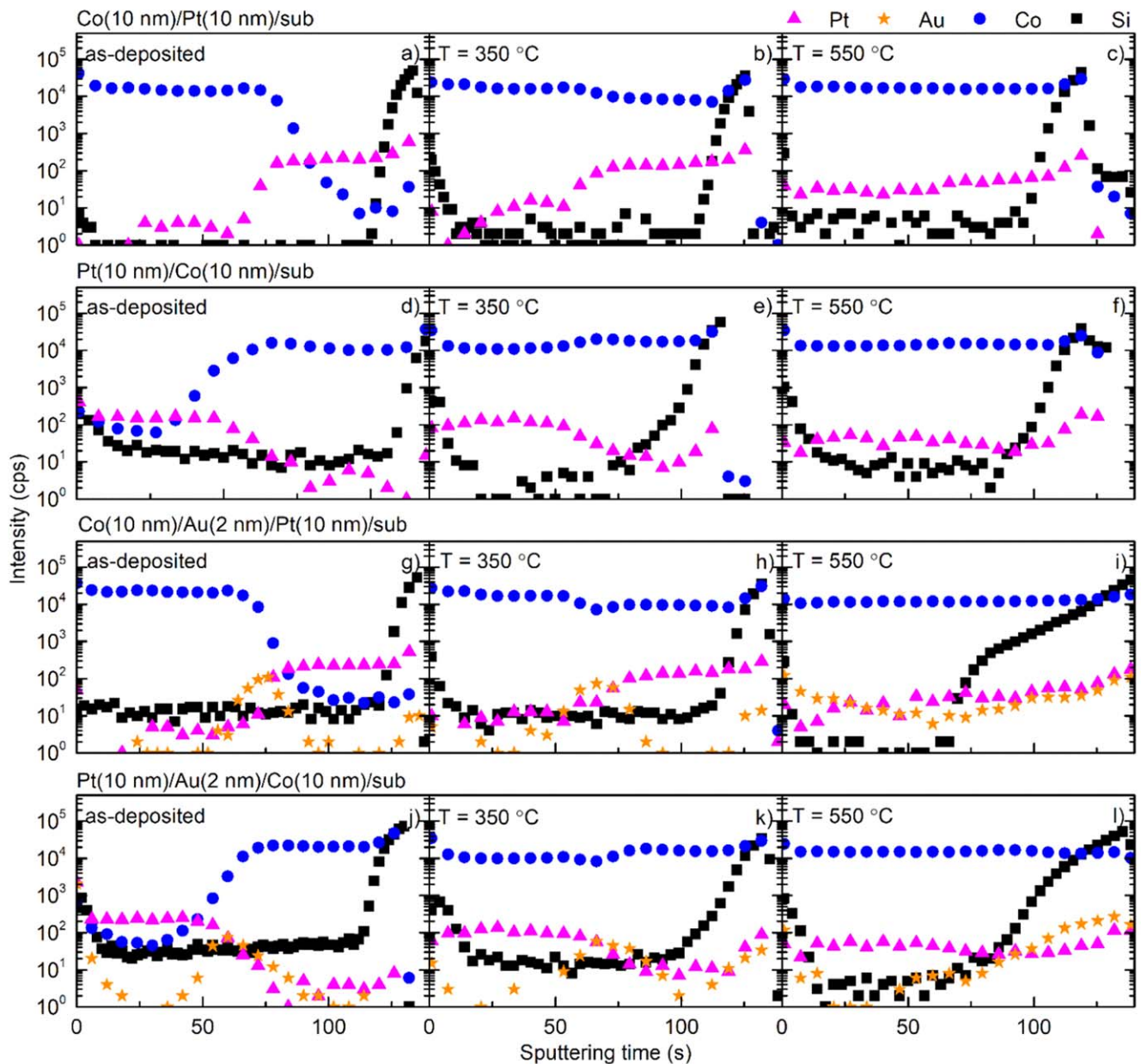
$T$ (°C)	Co/Pt/substrate				Pt/Co/substrate			
	Lattice parameter (Å)				Lattice parameter (Å)			
	$a$	$c$	$a$	$a$	$a, b$	$c$	$a, b, c$	$a, b, c$
	Co	Pt	Al-CoPt	Co	Pt	Al-CoPt	Al-CoPt	
as-dep.	2.40	4.25	3.92	—	—	—	3.92	—
150	2.66	4.20	3.80	—	—	—	3.93	—
250	2.40	4.10	3.96	—	—	—	3.90	—
350	2.46	3.79	3.90	3.80	—	—	3.89	3.79
450	—	—	3.76	3.68	—	—	3.90	3.74
550	—	—	—	3.71	—	—	—	3.71

$T$ (°C)	Co/Au/Pt/substrate					Pt/Au/Co/substrate				
	Lattice parameter (Å)					Lattice parameter (Å)				
	$a$	$c$	$a$	$a$	$a$	$a, b$	$c$	$a, b, c$	$a, b, c$	$a, b, c$
	Co	Pt	Au	Al-CoPt	Co	Pt	Au	Al-CoPt	Al-CoPt	
as-dep.	2.47	4.20	3.94	4.05	—	—	—	3.94	4.06	—
150	2.49	4.14	3.93	4.02	—	—	—	4.09	3.86	—
250	2.40	4.38	3.90	3.94	—	—	—	3.92	4.00	—
350	2.71	4.14	3.94	4.03	3.74	—	—	3.92	4.05	3.74
450	—	—	3.96	4.02	3.71	—	—	3.94	4.07	3.70
550	—	—	—	—	3.71	—	—	—	4.02	3.72

The SIMS profiles are displayed as a function of sputtering time, which is related to the film depth. It is worth noting that a certain amount of oxygen, nitrogen, and carbon atoms is always present on the surface of the samples, affecting the

sputtering process of the near-surface region [38]. For instance, the double mass of the nitrogen atom provides the mass similar to the mass of a single silicon atom. Moreover, oxygen at the surface could affect the sputtering rate at the



**Figure 4.** SIMS chemical depth profiles of the (a)–(c) Co(10 nm)/Pt(10 nm)/substrate, (d)–(f) Pt(10 nm)/Co(10 nm)/substrate, (g)–(i) Co(10 nm)/Au(2 nm)/Pt(10 nm)/substrate, and (j)–(l) Pt(10 nm)/Au(2 nm)/Co(10 nm)/substrate stacks in the as-deposited state and after annealing at 350 °C and 550 °C for 30 min.

initial stages, providing a strong surface signal from Si, which is just a measurement artifact.

From the SIMS chemical depth profiles, it can be seen that there are relatively sharp interfaces between the metallic layers in the as-deposited thin-film samples (figures 4(a), (d), (g), (j)), being in agreement with the TEM study (figure 3). Heat treatment at 350 °C leads to a redistribution of the chemical composition through the depth of the investigated stacks (figures 4(b), (e), (h), (k)). However, homogeneous distribution of the elements was not achieved after this treatment regime. It can be seen that the diffusion of Co to Pt occurs faster compared to the Pt transfer into the Co layer for each studied sample. This finding is in agreement with the

difference in melting temperatures of these metals, where the more fusible element diffuses faster (table 2) [42]. It should be noted that after annealing at 350 °C, Au remains almost unchanged in position compared to the as-deposited state (figures 4(h), (k)).

Annealing at 550 °C causes homogeneous distribution of Pt and Co through the depth of the investigated stacks (figures 4(c), (f), (i), (l)). Sample homogenization after this annealing regime was also confirmed by STEM imaging and EDXS-based element mapping (figure 5). The distribution of Au becomes more uniform in the Pt/Au/Co/substrate and Co/Au/Pt/substrate samples after this annealing regime (figures 4(i), (l)). Furthermore, Au surface segregation regions

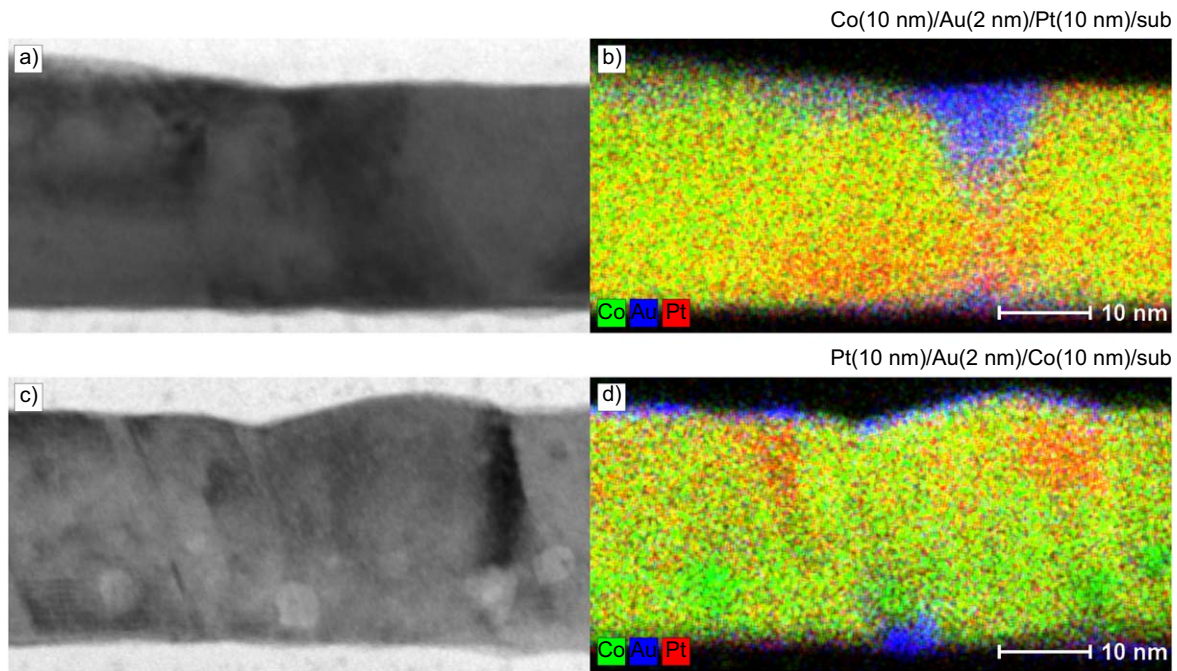


**Figure 5.** Cross-sectional BF-STEM images (a), (c) and corresponding EDXS-based element distribution maps (b), (d) of the samples annealed at 550 °C for 30 min. (a), (b) Co(10 nm)/Au(2 nm)/Pt(10 nm)/substrate and (c), (d) Pt(10 nm)/Au(2 nm)/Co(10 nm)/substrate.

**Table 2.** Melting temperatures and coefficients of the linear thermal expansion of SiO<sub>2</sub>, Si, Co, Pt, and Au.

Material	Melting temperature (°C) [44, 45]	Coefficient of linear thermal expansion (1/K) [44, 45]
SiO <sub>2</sub>	1710	$0.5 \times 10^6$
Si	1414	$2.6 \times 10^6$
Co	1495	$13.0 \times 10^6$
Pt	1768	$8.8 \times 10^6$
Au	1064	$14.2 \times 10^6$

can be seen in the SIMS profiles, being in agreement with the EDXS-based maps (figures 5(b), (d); see also supplementary information, figure S2). Finally, the distribution of Pt and Co through the depth of each of the investigated stacks is very similar. However, we note that the Au-containing samples have a larger thickness (2 nm thicker due to the presence of the Au layer) compared to the bilayer stacks. Thus, the diffusion length is larger for samples with Au. Therefore, the experimentally observed similar distributions of Pt and Co in all investigated stacks (SIMS data) could indicate the diffusion enhancement in the stacks with Au intermediate layers.

The SIMS technique allows us following the mass of the CoPt<sup>+</sup> complex ion. Since this complex ion forms only in case of the sputtering of a region containing both Pt and Co, the distribution of the intensity of this complex ion through the depth of the stacks is relevant for the analysis of the elements homogenization. Figure 6 displays the intensity distribution of CoPt<sup>+</sup> through the depth of each investigated stack after annealing at 250 °C, 350 °C, and 550 °C (corresponding depth distributions taken for all heat treatment regimes are given in the supplementary information, figure S7).

After annealing at 250 °C, the distribution of the elements is more uniform in the stacks with Co bottom layer (figure 6(a)). The same tendency remains after annealing at 350 °C: the Pt/Co/substrate and Pt/Au/Co/substrate stacks reveal more homogeneous structure compared to the Co/Pt/substrate and Co/Au/Pt/substrate samples (figure 6(b)). An increase of the annealing temperature to 550 °C leads to an almost similar distribution of the elements through the depth of each investigated thin-film sample, independent of the stacking (figure 6(c)). Thus, it can be concluded that a layer inversion has a pronounced effect on the diffusion rate during annealing up to a certain critical temperature. We take 550 °C as the critical temperature: below this temperature, mass transfer occurs primarily via grain boundaries, while starting from 550 °C, bulk diffusion dominates. This is in agreement with prior data on low-temperature homogenization: grain boundary diffusion dominates at lower temperatures, while the bulk mechanism dominates at higher ones [29]. Faster homogenization of the Pt/Co/substrate and Pt/Au/Co/substrate stacks at relatively low annealing temperature could be attributed to a smaller Pt grain size compared to the stacks with inverse layer setup, as was suggested by XRD. Smaller grain sizes lead to larger lengths within the grain boundary network, providing conditions for a faster mass transfer within the grain boundary diffusion mechanism. An additional factor affecting the diffusion rate could be related to mechanical stresses arising during the heat treatment due to the mismatch in the thermal expansion coefficients of the substrate and the contacting metal layer. These stresses are higher in case of the Co bottom layer since it provides a larger difference with the SiO<sub>2</sub>/Si substrate in terms of the thermal expansion coefficients compared to Pt (table 2). Mechanical stresses



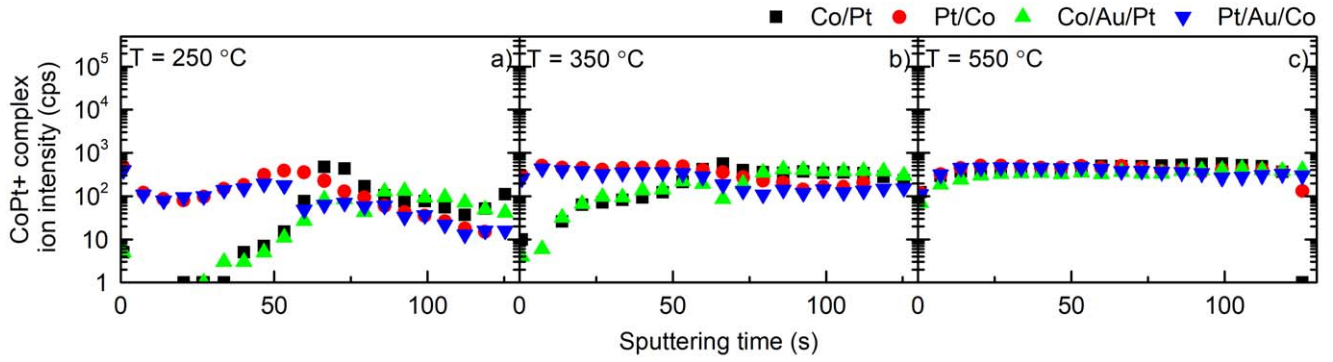


**Figure 6.** SIMS data revealing the dependence of the intensity of the  $\text{CoPt}^+$  complex ion on the sputtering time for the Co(10 nm)/Pt(10 nm)/substrate, Pt(10 nm)/Co(10 nm)/substrate, Co(10 nm)/Au(2 nm)/Pt(10 nm)/substrate, and Pt(10 nm)/Au(2 nm)/Co(10 nm)/substrate stacks after annealing in the range of 250 °C–550 °C for 30 min.

**Table 3.** Interface diffusion coefficients of Co and Pt atoms in the studied samples annealed at different temperatures. The estimation of the interface diffusion coefficient is based on the analysis of the SIMS profiles relying on the Hall–Morabito method.

Interface diffusion coefficient of Co into Pt				
$T$ (°C)	$D^{\text{Co/Pt}}$ ( $\text{cm}^2/\text{s}$ )	$D^{\text{Pt/Co}}$ ( $\text{cm}^2/\text{s}$ )	$D^{\text{Co/Au/Pt}}$ ( $\text{cm}^2/\text{s}$ )	$D^{\text{Pt/Au/Co}}$ ( $\text{cm}^2/\text{s}$ )
150	$1.95 \times 10^{-17}$	$8.34 \times 10^{-18}$	$3.77 \times 10^{-17}$	$3.53 \times 10^{-17}$
250	$5.10 \times 10^{-17}$	$5.72 \times 10^{-17}$	$6.08 \times 10^{-17}$	$5.79 \times 10^{-17}$
350	$4.34 \times 10^{-16}$	$1.62 \times 10^{-16}$	$8.99 \times 10^{-17}$	$1.83 \times 10^{-16}$

Interface diffusion coefficient of Pt into Co				
$T$ (°C)	$D^{\text{Co/Pt}}$ ( $\text{cm}^2/\text{s}$ )	$D^{\text{Pt/Co}}$ ( $\text{cm}^2/\text{s}$ )	$D^{\text{Co/Au/Pt}}$ ( $\text{cm}^2/\text{s}$ )	$D^{\text{Pt/Au/Co}}$ ( $\text{cm}^2/\text{s}$ )
150	$2.05 \times 10^{-17}$	$2.07 \times 10^{-17}$	$9.29 \times 10^{-18}$	$5.84 \times 10^{-17}$
250	$4.33 \times 10^{-17}$	$6.90 \times 10^{-17}$	$2.18 \times 10^{-17}$	$1.06 \times 10^{-16}$
350	$2.22 \times 10^{-16}$	$2.59 \times 10^{-16}$	$7.19 \times 10^{-17}$	$4.46 \times 10^{-16}$

could act as an additional driving force for the development of the diffusion processes [43].

In the following, we estimate the effective diffusion coefficients, which characterize the diffusion rate under both diffusion at the interface and grain boundary mechanisms, of Pt(Co) atoms into the Co(Pt) layer during annealing in the range of 150 °C–350 °C [46]:

$$D_{\text{eff}} = D + \left( \frac{f \delta}{l} \right) D_{\text{GB}}, \quad (1)$$

where  $D$  is the interface diffusion coefficient,  $D_{\text{GB}}$  is the grain boundary diffusion coefficient,  $f$  is the grain shape factor, which is equal to 1 for parallel columnar grains (this is the dominant microstructure of the magnetron-sputtered thin films [47]),  $l$  is the average grain size, which was estimated taking into account size of the scattering length calculated by the Scherrer equation, layers thickness ratio and results of the transmission electron microscopy study. It should be noted that estimation of the diffusion coefficients for samples annealed at temperatures higher than 350 °C becomes challenging due to the reactive character of the mass transfer, which leads to phase transitions.

Estimation of the interface diffusion parameters was performed via analysis of the SIMS chemical depth profiles by the ‘center-gradient’ Hall–Morabito method [48], using the following equation:

$$D = \frac{\left( \frac{G_0}{G_t} \right)^2 - 1}{4\pi G_0^2 t}, \quad (2)$$

where  $t$  is the annealing duration in seconds, and  $G_0$  and  $G_t$  are the concentration gradients obtained from the SIMS profiles of the as-deposited and annealed samples, respectively. These gradients were determined graphically by analyzing the broadening of the concentration profile. The diffusion coefficients estimated in such a way after relatively low annealing temperatures correspond to atoms exchange or vacancy diffusion mechanisms at the interface region. We note that the applicability of this approach for the diffusion characterization in nanoscale stacks was proven for various systems, see for instance [49, 50]. The estimated interface diffusion coefficients are summarized in table 3.

To estimate the grain boundary diffusion coefficients, we apply the Fisher–Whipple approach [51, 52]. The analysis was performed using linear regions of the chemical depth

**Table 4.** Grain boundary diffusion coefficients of Co and Pt atoms in the studied samples estimated from the SIMS profiles by the Fisher–Whipple method.

Grain boundary diffusion coefficient of Co into Pt				
$T$ (°C)	$D_{GB}^{Co/Pt}$ (cm <sup>2</sup> /s)	$D_{GB}^{Pt/Co}$ (cm <sup>2</sup> /s)	$D_{GB}^{Co/Au/Pt}$ (cm <sup>2</sup> /s)	$D_{GB}^{Pt/Au/Co}$ (cm <sup>2</sup> /s)
150	$2.49 \times 10^{-16}$	$6.84 \times 10^{-15}$	$6.03 \times 10^{-16}$	$1.16 \times 10^{-14}$
250	$3.64 \times 10^{-15}$	$2.26 \times 10^{-14}$	$3.64 \times 10^{-15}$	$1.90 \times 10^{-14}$
350	$1.09 \times 10^{-13}$	$1.00 \times 10^{-13}$	$7.99 \times 10^{-14}$	$1.14 \times 10^{-13}$

Grain boundary diffusion coefficient of Pt into Co				
$T$ (°C)	$D_{GB}^{Co/Pt}$ (cm <sup>2</sup> /s)	$D_{GB}^{Pt/Co}$ (cm <sup>2</sup> /s)	$D_{GB}^{Co/Au/Pt}$ (cm <sup>2</sup> /s)	$D_{GB}^{Pt/Au/Co}$ (cm <sup>2</sup> /s)
150	$1.10 \times 10^{-14}$	$8.09 \times 10^{-15}$	$7.88 \times 10^{-15}$	$1.24 \times 10^{-14}$
250	$1.25 \times 10^{-14}$	$2.15 \times 10^{-14}$	$1.28 \times 10^{-14}$	$1.23 \times 10^{-13}$
350	$3.47 \times 10^{-14}$	$1.01 \times 10^{-13}$	$2.89 \times 10^{-14}$	$1.40 \times 10^{-13}$

**Table 5.** Effective diffusion coefficients of Co and Pt atoms at temperatures 150 °C–350 °C.

Effective diffusion coefficient of Co into Pt				
$T$ (°C)	$D_{eff}^{Co/Pt}$ (cm <sup>2</sup> /s)	$D_{eff}^{Pt/Co}$ (cm <sup>2</sup> /s)	$D_{eff}^{Co/Au/Pt}$ (cm <sup>2</sup> /s)	$D_{eff}^{Pt/Au/Co}$ (cm <sup>2</sup> /s)
150	$1.92 \times 10^{-15}$	$4.31 \times 10^{-14}$	$4.21 \times 10^{-15}$	$8.73 \times 10^{-14}$
250	$3.07 \times 10^{-14}$	$1.42 \times 10^{-13}$	$2.92 \times 10^{-14}$	$1.44 \times 10^{-13}$
350	$7.56 \times 10^{-13}$	$6.35 \times 10^{-13}$	$5.04 \times 10^{-13}$	$6.74 \times 10^{-13}$

Effective diffusion coefficient of Pt into Co				
$T$ (°C)	$D_{eff}^{Co/Pt}$ (cm <sup>2</sup> /s)	$D_{eff}^{Pt/Co}$ (cm <sup>2</sup> /s)	$D_{eff}^{Co/Au/Pt}$ (cm <sup>2</sup> /s)	$D_{eff}^{Pt/Au/Co}$ (cm <sup>2</sup> /s)
150	$8.02 \times 10^{-16}$	$7.1 \times 10^{-16}$	$6.25 \times 10^{-16}$	$9.43 \times 10^{-16}$
250	$8.4 \times 10^{-16}$	$1.9 \times 10^{-15}$	$8.77 \times 10^{-16}$	$8.83 \times 10^{-15}$
350	$2.94 \times 10^{-15}$	$8.88 \times 10^{-15}$	$2.54 \times 10^{-15}$	$1.33 \times 10^{-14}$

profiles, which are replotted in coordinates  $\ln c = f(x^{\frac{6}{5}})$  at small concentration  $c$  and high distance  $x$  values. In this analysis, we assume that the SIMS intensity can be interpreted as the concentration and sputtering time as distance (i.e. thickness). According to this model, the triple product of grain boundary diffusion coefficient  $D_{GB}$ , grain boundary width  $\delta$ , and segregation factor  $K$  could be determined as:

$$K\delta D_{GB} = 0.61 \left( -\frac{\partial \ln c}{\partial x^{\frac{6}{5}}} \right)^{-\frac{5}{3}} \sqrt{\frac{4D}{t}}, \quad (3)$$

where  $D$  is the diffusion coefficient determined by the Hall–Morabito method (table 3). To calculate the grain boundary diffusion coefficients, the grain boundary width was assumed to be 0.75 nm based on the typical values of grain boundary widths in metals with values between 0.5 and 2 nm [29]. The segregation coefficient was taken as 1, assuming that there is no grain boundary segregation of the diffusants. The calculated grain boundary diffusion coefficients of Co and Pt atoms are summarized in table 4.

The calculated interface and grain boundary diffusion coefficients allowed us estimating the effective diffusion

parameters,  $D_{eff}$  (see equation (1)), which provide a more representative information concerning the diffusion rates. The effective diffusion coefficients of Co and Pt atoms are summarized in table 5. The estimated values of  $D_{eff}$  are in the range of  $10^{-16}$ – $10^{-13}$  cm<sup>2</sup> s<sup>-1</sup> for temperatures of 150 °C–350 °C, which are typical for low-temperature diffusion in thin films. We note that the estimated effective diffusion coefficients of Pt into Co thin films are found to be in the range of  $10^{-15}$  cm<sup>2</sup> s<sup>-1</sup>, which is about 2 orders of magnitude larger than the ones reported for diffusion of Pt into Co thick foils (i.e.  $3.0 \times 10^{-17}$  cm<sup>2</sup> s<sup>-1</sup> at 250 °C [53]). It can be seen that the larger melting temperature of Pt compared to Co (about 270 K difference for the respective bulk materials, see table 2) leads to the difference in their  $D_{eff}$  values of at least one order of magnitude. For the samples annealed at 350 °C, the diffusion rate is determined to be almost the same for each studied sample indicating a significant role of the bulk diffusion when processing thin films at this temperature.

The diffusion rates obtained based on the models of interfacial and grain boundary diffusion make it possible to estimate the respective contributions of the various mass

transfer mechanisms to the diffusion process in the studied stacks. In particular, analysis of the diffusion parameters summarized in table 3 (interface diffusion) and table 4 (grain boundary diffusion) indicates that the grain boundary diffusion model better describes the experimental SIMS data for samples processed at temperatures from 150 °C to 350 °C. For instance, within the grain boundary diffusion model, we can explain that Co diffusion develops faster in the stacks with Pt top layer. Furthermore, for most of the samples, the diffusion coefficients are correlated with the melting temperature of the respective materials and the diffusion in the stacks with an additional Au layer is faster compared to the bilayers. In contrast, the interface diffusion model predicts similar diffusion coefficients of Co and Pt atoms contradicting the analysis of SIMS spectra. Besides, this model does not capture the experimentally observed faster mass transfer for the stacks with Co bottom layer compared to the samples with Co top layer.

### 3.2. Magnetic characterization

$M$ – $H$  hysteresis loops of the as-deposited and annealed samples are shown in figure 7. The curves were measured at room temperature in an external magnetic field applied parallel ( $\parallel$ ) and perpendicular ( $\perp$ ) to the film surface. As can be seen from figures 7(a), (e), (i), (m), the as-deposited films reveal soft-magnetic properties with easy-plane anisotropy caused by the shape anisotropy. The hysteresis loops for the magnetic field applied along the hard-axis direction were also measured at higher fields to obtain the saturation magnetization (supplementary information, figure S8). Annealing in the range 150 °C–250 °C does not lead to significant changes in the coercivity (figure 8(a)). Despite the fact that annealing at 350 °C does not lead to phase transitions and structure homogenizations (see discussion above on XRD and SIMS measurements), all studied stacks show noticeable enhancement of coercivity and saturation magnetization after this heat treatment regime (figure 8(b)). Moreover, after annealing at 350 °C, the Au-containing three-layer stacks reveal a coercivity, which is higher than in the bilayer samples. It can be assumed that Au diffusion via grain boundaries leads to an isolation of ferromagnetic grains by the non-magnetic element, resulting in exchange decoupling between grains and, hence, in the coercivity enhancement. The coercive field increases for samples which were annealed at higher temperatures. In particular, the coercivity of the samples annealed at 550 °C increases by about 100 Oe compared to samples annealed at 350 °C (figures 7(b), (f), (j), (n) and 7(d), (h), (l), (p); 8(a)). However, the samples retain their easy-plane anisotropy. The maximum value of the achieved coercivity of  $\sim 360$  Oe was measured for the Co/Au/Pt/substrate stack. Since the formation of the chemically ordered  $L1_0$ -CoPt phase was not registered (see discussion of the XRD data), the observed coercivity enhancement is attributed to the short-range chemical ordering [38]. It should be noted that the observed magnetic characteristics agrees well with the data reported by Toyama *et al* [20]. The formation of the disordered A1-CoPt phase upon annealing of Pt/Co stacks

results in the enhancement of the saturation magnetization with its maximum for the samples annealed at 350 °C. This was attributed to an increase of the magnetic moments of Co and Pt atoms due to hybridization by Toyama *et al* [20]. For our samples, the mixing between the individual Co and Pt layers is observed after annealing at 350 °C. The intermixing is expected to result in the  $3d$ – $5d$  orbital hybridization between Co and Pt upon the formation of the disordered A1-CoPt phase.

We note that the values of the coercive field as well as the saturation magnetization and the easy-plane magnetic behavior agrees well with the previously published data. In particular, Toyama *et al* [20] reported an in-plane coercivity of about 300 Oe for the Pt/Co stacks annealed at 500 °C, which is similar to the 350 Oe observed for our samples annealed at 550 °C.

Ferromagnetic resonance spectra were recorded at room temperature at different directions of the external magnetic field with respect to the film normal. As an example, the angular dependences of the resonance fields for the Co/Au/Pt/substrate stack are presented in figure 9. The lines drawn through the data are fits of the experimental data to theoretical dependences calculated for magnetic films with effective magnetization:

$$4\pi M_{\text{eff}} = (N_{\perp} - N_{\parallel})\overline{M}_S - H_{a\perp}, \quad (4)$$

where  $\overline{M}_S$  is the mean saturation magnetization of the magnetic phase,  $N_{\perp}$  and  $N_{\parallel}$  are the perpendicular-to-the-film-plane and in-plane demagnetizing factors,  $H_{a\perp}$  is the perpendicular anisotropy field (surface anisotropy of Neel type, for instance). For all samples, maxima of the resonance fields were observed when the external magnetic field was perpendicular to the film plane (0° and 180°). This finding is in line with the outcome of the VSM study indicating that all samples possess easy-plane anisotropy. We note that in-plane ferromagnetic resonance measurements did not reveal any induced anisotropy in the film plane. Representative angular dependent FMR data obtained for the Co/Au/Pt stack annealed at 550 °C do not reveal any shift of the resonance field with the azimuthal angle (supplementary information, figure S9).

The effective magnetization values extracted from the angular dependencies of the resonance fields for the investigated stacks are given in figure 10. For each of the studied samples, an increase of the annealing temperature up to 450 °C results in a decrease of the effective magnetization. This lowering is related to both the increase of the stack volume occupied by the magnetic phase and the decrease of the demagnetizing factor  $N_{\perp}$  of the stack with nonuniform distribution of magnetic and nonmagnetic materials. For a homogeneous magnetic film, the demagnetizing factor is close to  $4\pi$ , while for a film consisting of structure elements revealing different magnetic properties, it becomes smaller and depends on the distribution and shape of magnetic and nonmagnetic inclusions (see, e.g. [54] for details). The most pronounced drop of the demagnetizing factor should be expected in the films where the diffusion takes place mainly along the grain boundaries, while the bulk diffusion promotes

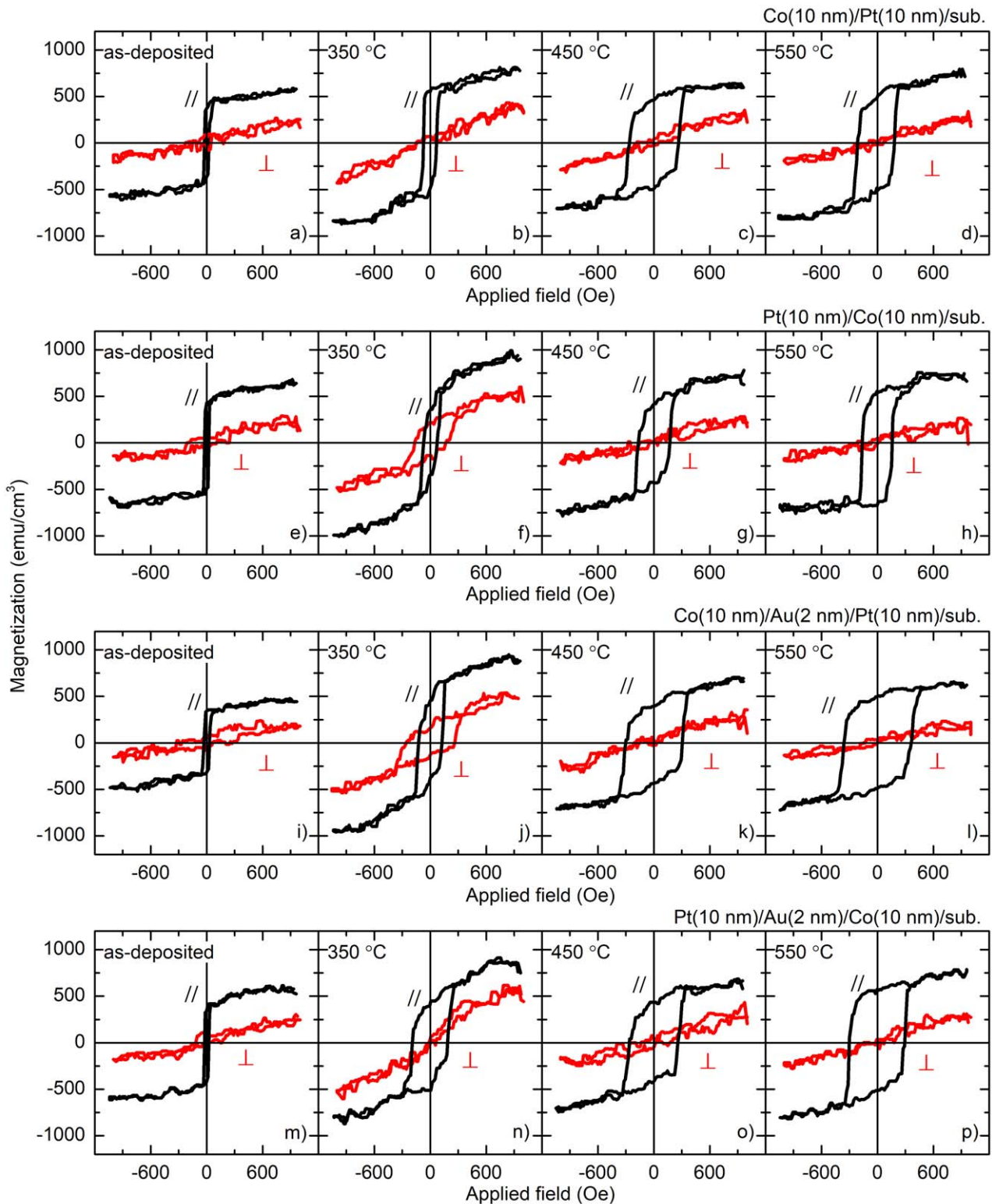


**Figure 7.**  $M-H$  hysteresis loops of the studied sample families after deposition and annealing in the range 350 °C–550 °C for 30 min.

homogenization of the magnetic parameters over the film volume. In this case, the demagnetizing factor should approach the value typical for a continuous film. For each of our samples, the grain boundary diffusion is the dominant mechanism at low annealing temperatures. The formation of heterogeneous magnetic-nonmagnetic structure is also

confirmed by the appearance of hysteresis for perpendicularly magnetized films annealed at 350 °C (figure 7).

A more rapid decrease of the effective magnetization is observed for the stacks with Co top layer. For these samples, the SIMS depth profiles reveal less intensive formation of  $\text{CoPt}^+$  complex ion at relatively low annealing temperatures,

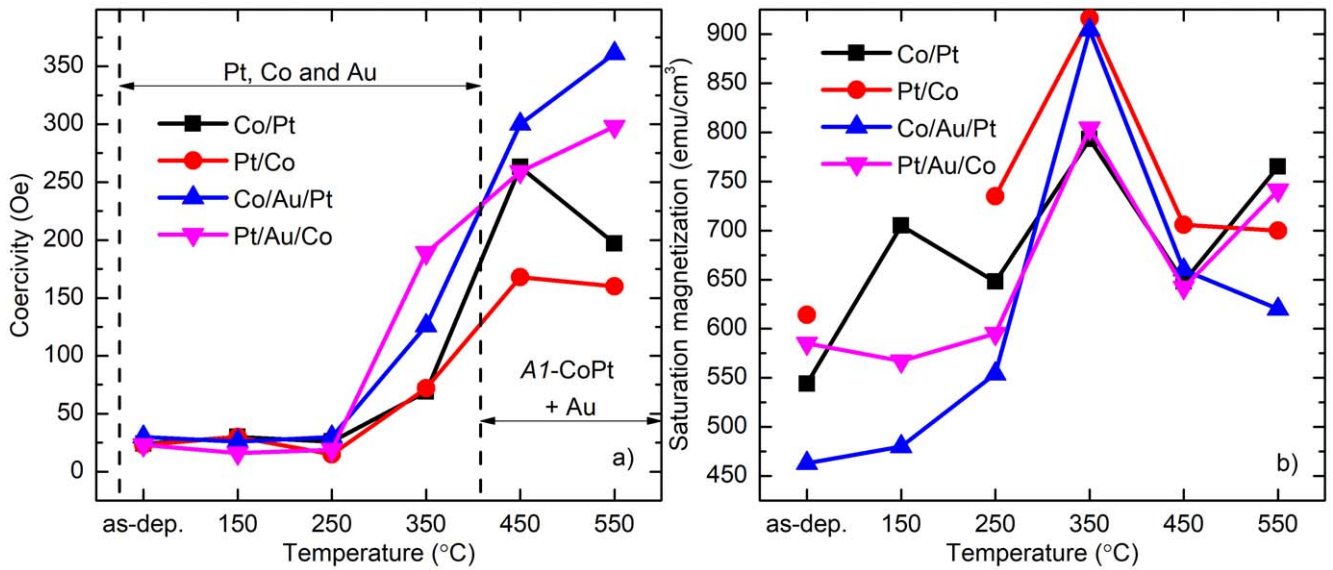


Figure 8.  $M$ - $H$  hysteresis loops of the studied sample families after deposition and annealing in the range 350 °C–550 °C for 30 min.

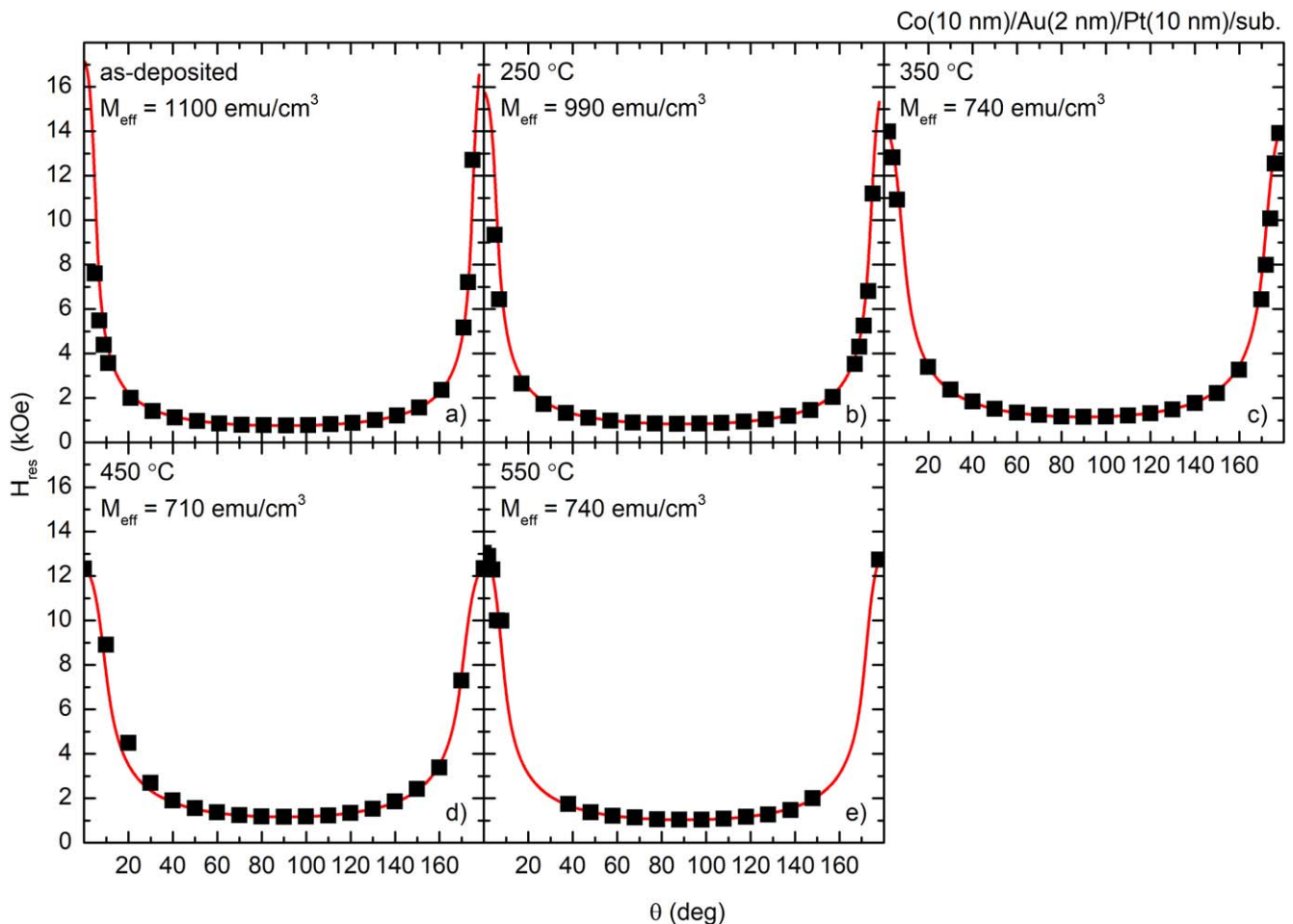
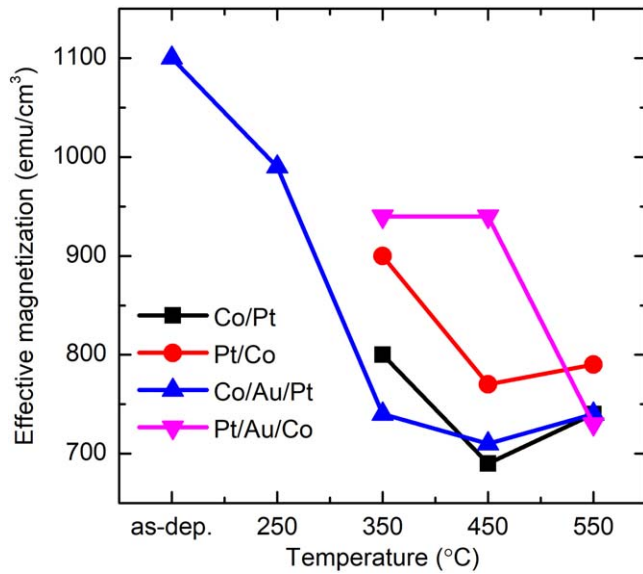


Figure 9. Dependences of the resonance fields as a function of the polar angle  $\theta$  (measured from the film normal) for the Co(10 nm)/Au(2 nm)/Pt(10 nm)/substrate stack annealed at different temperatures (symbols). Lines are fits according to equation (4).

providing conditions for the predominance of the grain boundary diffusion mechanism (figures 4 and 6). After annealing at 550 °C, the homogenization of the stacks takes

place resulting in the increase of the effective magnetization. This finding correlates well with the SIMS and TEM data showing homogeneous distribution of Co and Pt along the



**Figure 10.** Annealing temperature dependence of the effective magnetization for the studied samples.

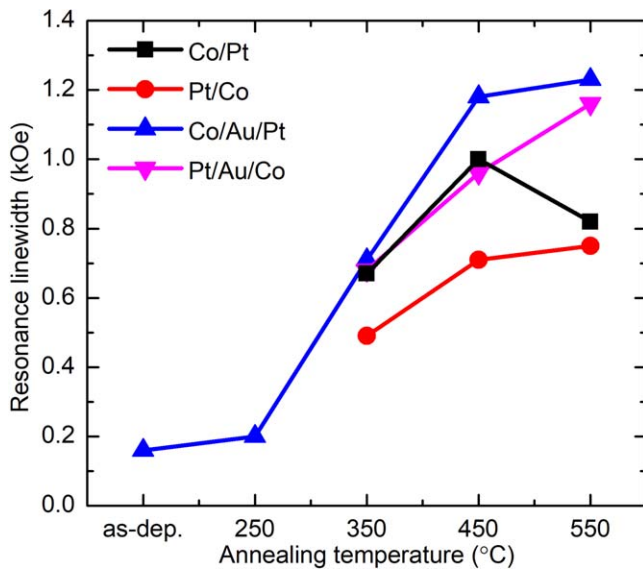


**Figure 11.** The annealing temperature dependence of ferromagnetic resonance linewidth for all studied samples.

thickness of the layer stacks. For the films with Au addition, an increase of the annealing temperature results in the enhancement of the coercivity as well as in the increase of the linewidth of the ferromagnetic resonance (figures 8 and 11). Both these factors indicate that the suppression of the exchange coupling between grains due to the presence of Au in grain boundaries leads to the increase of the role of the anisotropy of individual grains on the magnetic properties of the samples. In contrast, for the stacks without Au, annealing at 550 °C results in the decrease of the coercivity and narrowing of the width of the FMR peaks. In the films without Au, stronger intergrain coupling leads to averaging of the magnetic parameters over the film and a decrease of the role of individual grains in the overall magnetic behavior of the

samples (these films are magnetically more homogeneous). This results in lower coercivity and narrowing of the resonance linewidth.

We note different dependencies of the saturation magnetization measured by VSM and the effective magnetization determined from FMR on the annealing temperature (compare figures 8(b) and 10). For the as-deposited films, the FMR data reveal an effective magnetization which is close to the saturation magnetization of Co films. It is important to note that the saturation magnetization measured by VSM is the magnetic moment of a film divided by the full stack volume. Taking into account the continuous structure of the Co layer, the saturation magnetization of this layer is very close to the saturation magnetization obtained from FMR. For instance, for the Co/Au/Pt stack, these values are 1250 emu cm<sup>-3</sup> (VSM) and 1100 emu cm<sup>-3</sup> (FMR). The discrepancy in these values can be caused by a partial diffusion of Co during the deposition process, the formation of surface anisotropy in such layered structures (see equation (4)), or some error in the determination of the measured stack volume. The same situation is observed for the stacks annealed at relatively high temperature revealing practically a continuous CoPt alloy structure (see figures 5, 6). In this case, the saturation magnetizations and the effective magnetizations are practically the same with values in the range of 700–800 emu cm<sup>-3</sup>. The main difference between the saturation magnetization (VSM) and effective magnetization (FMR) is observed for the stacks annealed at intermediate temperatures, especially at 350 °C. The VSM-measured saturation magnetization shows the maximum value after this treatment. However, the effective magnetization for these stacks is much lower compared to the as-deposited samples. Taking into account a rather homogeneous distribution of Co after annealing at this temperature and neglecting the contribution of the anisotropy, it became possible to determine the demagnetizing factor of the stacks using equation (4). By using the value of the saturation magnetization determined from the VSM data, the demagnetizing factor ( $N_{\perp} - N_{\parallel}$ ) was estimated to be about 8–10, which is typical for discontinuous or granular films [54]. This means that a significant amount of magnetic phase is separated by nonmagnetic inclusions. This finding is in line with the assumption that Co diffuses along Pt grain boundaries at intermediate annealing temperatures. Taking into account that there is a close-to homogeneous distribution of the elements through the depth of the stack annealed at 550 °C, the resonance line broadening is determined by the anisotropy distribution [55]. Hence, the FMR linewidth can be used as an estimate for the magnetic anisotropy field:  $\sim 800$  Oe ( $\sim 3 \times 10^5$  erg cm<sup>-3</sup>) for the stacks without an additional Au layer and  $\sim 1200$  Oe ( $\sim 4.5 \times 10^5$  erg cm<sup>-3</sup>) for the Au-containing samples. These values are lower than those expected for the A1-CoPt phase ( $\sim 1 \times 10^6$  erg cm<sup>-3</sup> [56]), which is due to the fine grain structure of the investigated films and strong exchange intergrain interaction, resulting in a decrease of the net anisotropy values. This fact also explains the difference in the anisotropy values for the stacks with and without Au layer, since Au presence leads to the decrease of the intergrain exchange accompanied by the corresponding enhancement of

**Table 6.** Anisotropy field of the studied samples evaluated by various approaches.

Annealing temperature	Sample	$H_a$ calculated using equation (5), Oe	$H_a$ calculated using equation (6), Oe	$H_a$ extracted from the FMR linewidth, Oe
as-deposited	Co/Pt	80	85	
	Pt/Co	80	90	
	Co/Au/Pt	90	75	
	Pt/Au/Co	80	80	
350 °C	Co/Pt	220	190	
	Pt/Co	230	190	
	Co/Au/Pt	410	290	
	Pt/Au/Co	600	400	
450 °C	Co/Pt	810	700	
	Pt/Co	530	350	
	Co/Au/Pt	940	760	
	Pt/Au/Co	840	650	
550 °C	Co/Pt	630	520	800
	Pt/Co	500	630	750
	Co/Au/Pt	1130	1100	1250
	Pt/Au/Co	940	920	1150

the anisotropy. This conclusion agrees with the VSM data, revealing an increase of coercivity for the Au-containing samples. Alternatively, the anisotropy field of the investigated samples can be estimated based on the Stoner-Wohlfarth model for coherent magnetization rotation. Within this model for an assembly of noninteracting particles with cubic anisotropy (see, e.g. [57]), the link between the coercive field  $H_c$  and anisotropy field  $H_a$  is given by the expression:

$$H_c = 0.32H_a. \quad (5)$$

Based on the experimental data for the coercive field shown in figure 8(a), the anisotropy field is calculated and summarized in table 6. Furthermore, we evaluated the anisotropy field based on the analysis of hysteresis losses,  $E$ :

$$E = \int (M(H)_{\parallel} - M(H)_{\perp}) dH. \quad (6)$$

For samples with random orientation of the cubic anisotropy axes,  $E \sim 2K_c$ , where  $K_c = H_a M_s / 2$  - constant of the cubic anisotropy. Based on the analysis of the in-plane and out-of-plane hysteresis loops (figure 7 and supplementary information, figure S8), the anisotropy field can be estimated relying on equation (6), as summarized in table 6. We note that the anisotropy field values estimated by various approaches (table 6) are in reasonable agreement. The difference in the absolute values is caused by the fact that for correct determination of the anisotropy field it is necessary to take into account the real distribution of the anisotropy field as well as magnetostatic and exchange interactions between the grains of the investigated samples. The cubic anisotropy constant can be estimated based on the values given for the anisotropy field in table 6.

#### 4. Conclusions

In this work, we investigated the thermally induced diffusion and diffusion-controlled evolution of Pt/Co-based heterostructures. The effect of the layer stacking (Pt(10 nm)/Co(10 nm)/substrate versus Co(10 nm)/Pt(10 nm)/substrate) and the introduction of an additional 2 nm thick Au intermediate layer were explored by systematic structural (XRD, TEM), chemical (SIMS), and magnetic (VSM, FMR) analyzes of the samples annealed in vacuum with a constant duration in the temperature range of 150 °C–550 °C. The diffusion parameters (interfacial, grain boundary, and effective) were quantified. The obtained values of the effective diffusion constants are in the range of  $10^{-16}$ – $10^{-13}$  cm<sup>2</sup> s<sup>-1</sup> for temperatures of 150 °C–350 °C. At temperatures below 350 °C, the dominant mechanism of mass transfer is determined to be the grain boundary diffusion. It was found that diffusion is significantly affected by the stacking sequence up to some critical annealing temperature, which is taken to be 350 °C. This finding was attributed to the different grain size and, as a result, the different length of the grain boundary network as well as to various levels of mechanical stresses in the stacks with inverted order of the layers. The insertion of an Au intermediate layer results in the enhancement of both homogenization rate and coercivity of the annealed samples due to the lowering of the intergrain exchange coupling caused by the grain boundary diffusion of Au. The in-plane coercivity was increased 1.75 times for Co/Au/Pt and 2 times for Pt/Au/Co after annealing at 550 °C compared to the samples without an additional Au layer after similar heat treatment. As the formation of the chemically ordered  $L1_0$ -CoPt was not detected, the increase of the samples coercivity field from  $\sim 25$  Oe (as-deposited state) to  $\sim 350$  Oe (after annealing at 550 °C for 30 min) was attributed to the short-range chemical ordering.




## Acknowledgments

The work was supported in part by the Ministry of Education and Science of Ukraine (Project 0123U101257), the National Research Foundation of Ukraine (Project 02.2020/0261), the German Research Foundation (Grant #MA5144/33-1, #VE267/9-1, #VE948/5-1), and the European Commission (project REGO; ID: 101070066). The authors thank Romy Aniol and Andreas Worbs for TEM specimen preparation. Furthermore, the use of the HZDR Ion Beam Center TEM facilities and the funding of TEM Talos by the German Federal Ministry of Education and Research (BMBF), Grant No. 03SF0451, in the framework of HEMCP are acknowledged.

## Data availability statement

All data that support the findings of this study are included within the article (and any supplementary files).

## ORCID iDs

René Hübner  <https://orcid.org/0000-0002-5200-6928>  
 Denys Makarov  <https://orcid.org/0000-0002-7177-4308>  
 Igor Vladymyrskiy  <https://orcid.org/0000-0002-2106-9176>

## References

- [1] Cuchet L, Rodmacq B, Auffret S, Sousa R C, Prejbeanu I L and Dieny B 2016 Perpendicular magnetic tunnel junctions with a synthetic storage or reference layer: a new route towards Pt- and Pd-free junctions *Sci. Rep.* **6** 21246
- [2] Fan T, Khang N H D, Nakano S and Hai P N 2022 Ultrahigh efficient spin orbit torque magnetization switching in fully sputtered topological insulator and ferromagnet multilayers *Sci. Rep.* **12** 2998
- [3] Nam N H, Trung T T, Kien L M, Hong T T, Hai N H and Luong N H 2023 Tunable magnetic properties of CoPt nanoparticles: Impacts of phase coexistence and thermal annealing *J. Sci.: Adv. Mater. Devices* **8** 100589
- [4] Crisan A, Vasiliu F, Mercioniu I, Bartha C, Enculescu M and Crisan O 2018 Annealing-induced high ordering and coercivity in novel  $L1_0$  CoPt-based nanocomposite magnets *Metals* **8** 466
- [5] Li Z W, Jiao J Y, Luo Z, Ma T Y, Qiao L, Wang Y, Wang T and Li F S 2019 Microstructure and magnetic properties of exchange-coupled  $\text{Co}_{72}\text{Pt}_{28}/\text{Pt}/\text{Co}_{81}\text{Ir}_{19}$  composite media for perpendicular magnetic recording *J. Supercond. Novel Magn.* **32** 2229–33
- [6] Li W, Harumoto T, Nakamura Y and Shi J 2021 Primitive exchange coupling in CoPt/MnN layered structures: Exchange coupling established during deposition *J. Magn. Mater.* **538** 168331
- [7] Lan T T B, Jane H-J, Ding W-Y, Huang S-Y, Fang L-H, Wu J-C and Sun A A-C 2023 Huge giant-magnetoresistance of Co/Ru/ $L1_1$ -CoPt multi-layer pseudo-spin valve *J. Alloys Compd.* **938** 168441
- [8] Qiu S, Harumoto T, Nakamura Y and Shi J 2022 Magneto-transport properties of perpendicular magnetization CoPt/ $\text{VO}_2$  bilayer films grown on glass substrate *Surf. Coat. Technol.* **436** 128312
- [9] Dong Y N, Zhao X N, Wang W, Chen Y X, Bai L H, Yan S S and Tian Y F 2022 Room temperature manipulation of exchange bias in magnetic heterojunctions *J. Magn. Mater.* **559** 169546
- [10] Gupta S, Rortais F, Ohshima R, Ando Y, Endo T, Miyata Y and Shiraiishi M 2021 Approaching barrier-free contacts to monolayer  $\text{MoS}_2$  employing [Co/Pt] multilayer electrodes *NPG Asia Mater.* **13** 13
- [11] Shirokura T, Fan T, Khang N H D, Kondo T and Hai P N 2022 Efficient spin current source using a half-Heusler alloy topological semimetal with back end of line compatibility *Sci. Rep.* **12** 2426
- [12] Yamane H 2021 Magneto-optical surface plasmon resonances on perpendicular magnetic thin films consisting of CoPt/ZnO/Ag stacked nanolayers *Japan. J. Appl. Phys.* **60** SCCC01
- [13] Yamane H, Yanase S, Hasegawa T, Kobayashi M and Yasukawa Y 2022 Polarization transformation and destructive interference on subwavelength magnetic domains in magneto-plasmonic systems *Sci. Rep.* **12** 13871
- [14] Dugato D A, Brandão J, Béron F, da Silva R B, Flewett S, Shapiro D A, Cezar J C, Dorneles L S and Mori T J A 2023 Proximity induced moment at Pt/Co interfaces and isolated skyrmion bubble stabilization at zero magnetic field *J. Magn. Mater.* **566** 170305
- [15] Chen Z et al 2021 Current-induced magnetization switching in a chemically disordered  $A1$  CoPt single layer *Appl. Phys. Express* **14** 033002
- [16] Aledealat K, Aladerah B and Obeidat A 2023 Study of structural, electronic, and magnetic properties of  $L1_0$ -ordered CoPt and NiPt: an *ab initio* calculations and Monte Carlo simulation *Solid State Commun.* **363** 115112
- [17] Lim S T, Tran M, Chenchen J W, Ying J F and Han G 2015 Effect of different seed layers with varying Co and Pt thicknesses on the magnetic properties of Co/Pt multilayers *J. Appl. Phys.* **117** 17A731
- [18] Szívós J, Pothorszky S, Soltys J, Serényi M, An H, Gao T, Deák A, Shi J and Sáfrán G 2018 CoPt/TiN films nanopatterned by RF plasma etching towards dot-patterned magnetic media *Appl. Surf. Sci.* **435** 31–8
- [19] Ewing J, Wang Y and Arnold D P 2017 High-current-density electrodeposition using pulsed and constant currents to produce thick CoPt magnetic films on silicon substrates *AIP Adv.* **8** 056711
- [20] Toyama R, Kawachi S, Iimura S, Yamaura J-I, Murakami Y, Hosono H and Majima Y 2020 Formation of  $L1_0$ -ordered CoPt during interdiffusion of electron-beam-deposited Pt/Co bilayer thin films on Si/SiO<sub>2</sub> substrates by rapid thermal annealing *Mater. Res. Express* **7** 066101
- [21] Li M, Li Q, Zhang S, Fu J, Gu F, Ma W, Shi H and Yu G 2022 Magnetic properties and microstructural analyses of Pt/Co/Gd<sub>2</sub>O<sub>3</sub> films *Vacuum* **205** 111410
- [22] Sun A-C, Yuan F-T, Hsu J-H and Lee H Y 2009 Evolution of structure and magnetic properties of sputter-deposited CoPt thin films on MgO(111) substrates: Formation of the  $L1_1$  phase *Scr. Mater.* **61** 713–6
- [23] Withrow S P, White C W, Budai J D, Boatner L A, Sorge K D, Thompson J R and Kalyanaraman R 2003 Ion beam synthesis of magnetic Co–Pt alloys in Al<sub>2</sub>O<sub>3</sub> *J. Magn. Mater.* **260** 319–29
- [24] Rakshit R K, Bose S K, Sharma R and Budhani R C 2006 Giant coercivity nanodots and fractals in CoPt films grown on (001) SrTiO<sub>3</sub> using pulsed laser deposition *Appl. Phys. Lett.* **89** 202511



- [25] Ohtake M, Ouchi S, Kirino F and Futamoto M 2012 L1 ordered phase formation in FePt, FePd, CoPt, and CoPd alloy thin films epitaxially grown on MgO(001) single-crystal substrates *J. Appl. Phys.* **111** 07A708
- [26] Ohtake M, Itabashi A, Futamoto M, Kirino F and Inaba N 2014 Control of *c*-axis orientation of L1<sub>0</sub> ordered FePt, CoPt, and FePd alloy thin films deposited on MgO(001) substrates *IEEE Trans. Magn.* **50** 1–4
- [27] Makarov D, Klimenta F, Fischer S, Liscio F, Schulze S, Hietschold M, Maret M and Albrecht M 2009 Nonepitaxially grown nanopatterned Co–Pt alloys with out-of-plane magnetic anisotropy *J. Appl. Phys.* **106** 114322
- [28] Makarov D, Bermúdez-Ureña E, Schmidt O G, Liscio F, Maret M, Brombacher C, Schulze S, Hietschold M and Albrecht M 2008 Nanopatterned CoPt alloys with perpendicular magnetic anisotropy *Appl. Phys. Lett.* **93** 153112
- [29] Beke D L, Kaganovskii Y and Katona G L 2018 Interdiffusion along grain boundaries—diffusion induced grain boundary migration, low temperature homogenization and reactions in nanostructured thin films *Prog. Mater. Sci.* **98** 625–74
- [30] Katona G L, Safonova N Y, Ganss F, Mitin D, Vladymyrskyi I A, Sidorenko S I, Makogon I N, Beddies G, Albrecht M and Beke D L 2015 Diffusion and solid state reactions in Fe/Ag/Pt and FePt/Ag thin-film systems *J. Phys. D: Appl. Phys.* **48** 175001
- [31] Abedi M, Asadi A, Sovizi S, Moskovskikh D, Vorotilo S and Mukasyan A 2022 Influence of pulsed direct current on the growth rate of intermetallic phases in the Ni–Al system during reactive spark plasma sintering *Scr. Mater.* **216** 114759
- [32] Kostka A, Naujoks D, Oellers T, Salomon S, Somsen C, Öztürk E, Savan A, Ludwig A and Eggeler G 2022 Linear growth of reaction layer during *in situ* TEM annealing of thin film Al/Ni diffusion couples *J. Alloys Compd.* **922** 165926
- [33] Deng Z, Xu K, Tian Y, Lou M, Xue R, Zhang L, Liu L and Chang K 2022 Experimental investigation and thermodynamic re-assessment of the Ti–Zn system and atomic mobility of its bcc phase *Calphad* **76** 102392
- [34] Zhang C Q and Liu W 2019 Non-parabolic Al<sub>3</sub>Ti intermetallic layer growth on aluminum-titanium interface at low annealing temperatures *Mater. Lett.* **256** 126624
- [35] Vladymyrskyi I A *et al* 2015 Low-temperature formation of the FePt phase in the presence of an intermediate Au layer in Pt/Au/Fe thin films *J. Phys. D: Appl. Phys.* **49** 035003
- [36] Toyama R, Kawachi S, Yamaura J-I, Murakami Y, Hosono H and Majima Y 2020 Ti underlayer effect on the ordering of CoPt in (Co/Pt)<sub>4</sub> multilayer thin films on Si/SiO<sub>2</sub> substrates *Japan. J. Appl. Phys.* **59** 075504
- [37] Toyama R, Kawachi S, Yamaura J-I, Murakami Y, Hosono H and Majima Y 2022 Large coercivity of 13 kOe in L1<sub>0</sub>-ordered CoPt on Si/SiO<sub>2</sub> substrates by hydrogen annealing *Japan. J. Appl. Phys.* **61** 065002
- [38] Pedan R *et al* 2022 Homogenization and short-range chemical ordering of Co–Pt alloys driven by the grain boundary migration mechanism *J. Phys. D: Appl. Phys.* **55** 405004
- [39] Tynkova A, Katona G L, Langer G A, Sidorenko S I, Voloshko S M and Beke D L 2014 Formation of Cu<sub>x</sub>Au<sub>1-x</sub> phases by cold homogenization of Au/Cu nanocrystalline thin films *Beilstein J. Nanotechnol.* **5** 1491–500
- [40] Katona G L and Gulyas S 2020 *Grain Boundary Diffusion Dominated Mixing and Solid State Reactions in Magnetic Thin Films* (Springer) pp 145–62
- [41] Toyama R, Kawachi S, Yamaura J-I, Fujita T, Murakami Y, Hosono H and Majima Y 2022 Nanostructure-induced L1<sub>0</sub>-ordering of twinned single-crystals in CoPt ferromagnetic nanowires *Nanoscale Adv.* **4** 5270–80
- [42] Tiwari G P and Mehrotra R S 2008 Diffusion and melting *Defect Diffusion Forum* **279** 23–37
- [43] Chen C, Kitakami O, Okamoto S and Shimada Y 2000 Ordering and orientation of CoPt/SiO<sub>2</sub> granular films with additive Ag *Appl. Phys. Lett.* **76** 3218–20
- [44] Lide D R (ed) 1998 *Chemical Rubber Company Handbook of Chemistry and Physics* 79th edn (CRC Press)
- [45] Kaye G W C and Laby T H 1993 *Tables of Physical and Chemical Constants* 15th edn (Longman)
- [46] Hart E W 1957 On the role of dislocations in bulk diffusion *Acta Metall.* **5** 597
- [47] Thompson C V 1990 Grain growth in thin films *Annu. Rev. Mater. Sci.* **20** 245–68
- [48] Hall P M and Morabito J M 1976 A formalism for extracting diffusion coefficients from concentration profiles *Surf. Sci.* **54** 79–90
- [49] Tynkova A, Katona G L, Erdelyi G, Daroczi L, Oleshkevych A I, Vladymyrskyi I A, Sidorenko S I, Voloshko S M and Beke D L 2015 Nanoscale diffusion in Pt/<sup>56</sup>Fe/<sup>57</sup>Fe thin-film system *Thin Solid Films* **589** 173–81
- [50] Chakraborty J, Welzel U and Mittemeijer E J 2010 Mechanisms of interdiffusion in Pd–Cu thin film diffusion couples *Thin Solid Films* **518** 2010–20
- [51] Fisher J C 1951 Calculation of diffusion penetration curves for surface and grain boundary diffusion *J. Appl. Phys.* **22** 74–7
- [52] Whipple R T P 1954 CXXXXVIII. Concentration contours in grain boundary diffusion. the london, edinburgh, and dublin *Phil. Magazine J. Sci.* **45** 1225–36
- [53] Raiser D, Rossini I and Sens J C 1994 Diffusion parameters at the Pt–Co interface *Nucl. Instrum. Methods Phys. Res. B* **89** 183–5
- [54] Netzelmann U 1990 Ferromagnetic resonance of particulate magnetic recording tapes *J. Appl. Phys.* **68** 1800–7
- [55] Valstyn E P, Hanton J P and Morrish A H 1962 Ferromagnetic resonance of single-domain particles *Phys. Rev.* **128** 2078–87
- [56] Rohart S, Raufast C, Favre L, Bernstein E, Bonet E, Wernsdorfer W and Dupuis V 2007 Interface effect on the magnetic anisotropy of CoPt clusters *J. Magn. Magn. Mater.* **316** e355–9
- [57] Ibusuki T, Kojima S, Kitakami O and Shimada Y 2001 Magnetic anisotropy and behaviors of Fe nanoparticles *IEEE Trans. Magn.* **37** 2223–5